Strong Orientation-Dependent Spin-Orbit Torque in Thin Films of the Antiferromagnet Mn_2Au

X. F. Zhou,[1] J. Zhang,[2] F. Li,[1] X. Z. Chen,[1] G. Y. Shi,[1] Y. Z. Tan,[1] Y. D. Gu,[1] M. S. Saleem,[1] H. Q. Wu,[3] F. Pan,[1] and C. Song[1,*]

[1]*Key Laboratory of Advanced Materials (MOE), School of Materials Science and Engineering, Tsinghua University, Beijing 100084, China*

[2]*School of Physics and Wuhan National High Magnetic Field Center, Huazhong University of Science and Technology, Wuhan 430074, China*

[3]*Institute of Microelectronics, Tsinghua University, Beijing 100084, China*

(Received 13 December 2017; published 18 May 2018)

Antiferromagnets with zero net magnetic moment, strong anti-interference, and ultrafast switching speed are potentially competitive in high-density information storage. The body-centered tetragonal antiferromagnet Mn_2Au with opposite-spin sublattices is a unique metallic material for Néel-order spin-orbit-torque (SOT) switching. We investigate the SOT switching in quasiepitaxial (103), (101) and (204) Mn_2Au films prepared by a simple magnetron sputtering method. We demonstrate current-induced antiferromagnetic moment switching in all of the prepared Mn_2Au films by using a short current pulse at room temperature, whereas differently oriented films exhibit distinguished switching characters. A direction-independent reversible switching is attained in Mn_2Au (103) films due to negligible magnetocrystalline anisotropy energy, while for Mn_2Au (101) and (204) films, the switching is invertible with the current applied along the in-plane easy axis and its vertical axis, but it becomes attenuated seriously during initial switching circles when the current is applied along the hard axis because of the existence of magnetocrystalline anisotropy energy. Besides the fundamental significance, the strong orientation-dependent SOT switching, which is not realized, irrespective of ferromagnet and antiferromagnet, provides versatility for spintronics.

DOI: 10.1103/PhysRevApplied.9.054028

I. INTRODUCTION

Alternate arrangement of magnetic moments on adjacent atoms makes antiferromagnets (AFMs) show zero net magnetization without a stray field and resultant immunity to external perturbations [1]. After more than a half century of passive role of AFM for the exchange bias effect at the interface coupled to ferromagnets (FMs) [2], antiferromagnet spintronics have emerged as a fascinating research area and stimulated intense interest due to their potential for ultrafast and ultrahigh-density spintronics [1,3–7]. Much beyond the static behavior of an AFM as supporting layer in spin valves and magnetic tunnel junctions [8], different methods have been demonstrated to manipulate the AFM spins in AFM-based memory resistors [9] and tunneling anisotropic magnetoresistance [6,10], taking advantage of FM switching [11], field cooling [12], strain [13], the electric field [14–18], and the electric current, which was realized recently [5,19,20].

Controlling magnetism by current—namely, spin-transfer torque [21] and spin-orbit torque (SOT) [22–24]—manifests great superiority for low-power spintronics, and favorable progress has been made in FM systems and relevant magnetic random-access memory. SOT has recently been used for the switching of both synthetic antiferromagnets [25,26] and antiferromagnetic Cu-Mn-As [5,20], mainly attributed to the role of fieldlike torque $dM_{A,B}/dt \sim M_{A,B} \times p_{A,B}$, where the effective field proportional to $p_A = -p_B$ acting on the spin-sublattice magnetizations $M_{A,B}$ [4,5]. SOT in collinear antiferromagnets has been studied in bulk Mn_2Au tight-binding models. The two Mn_2Au crystal sublattices connected by inversion and microscopic calculations based on the Kubo formula show that the Néel SOT in Mn_2Au is of predominantly fieldlike character [4,24,27]. And current-driven SOT is also theoretically predicted in the easily prepared metallic antiferromagnet Mn_2Au, with similar opposite-spin sublattices to Cu-Mn-As [1,4,24,27], which shows a high Néel temperature above 1000 K [27], higher conductivity, and a resultant lower energy dissipation for application compared to the arsenic-based AFM, demonstrating the pressing demand and great significance of the study of SOT in Mn_2Au.

The orientation-dependent spin-orbit interaction and the corresponding SOT have been commonly ignored mainly because the perpendicular magnetic anisotropy of the ferromagnetic stacks is persistently limited by a certain

*songcheng@mail.tsinghua.edu.cn

preferred orientation, such as (111)-oriented Pt/Co and (100)-oriented Ta/(Co, Fe)B. Recently, a facet-dependent spin Hall angle was observed in the triangular antiferromagnet $IrMn_3$, which provides efficient charge-to-spin current conversion and a concomitant spin current propagating from the antiferromagnetic into an adjacent ferromagnetic material [28]. Considering that the fieldlike torque in AFMs with opposite-spin sublattices is not restricted to a certain crystalline orientation, orientation-dependent magnetic switching is expected in this scenario, which has not been realized in either ferromagnets or antiferromagnets, providing a versatile candidate for spintronics. Compared to polycrystalline Mn_2Au films grown by molecular beam epitaxy [29,30] and partially (001)-oriented Mn_2Au films deposited by sputtering [31], the experiments below attain quasiepitaxial (103), (101), and (204) Mn_2Au films, and they demonstrate the orientation-dependent Néel-order spin-orbit-torque switching in single-layer Mn_2Au films with different switching features for different orientations.

II. METHODS

We grow 40-nm-thick (103)-, (101)-, and (204)-oriented Mn_2Au films on single-crystal MgO(111), $SrTiO_3$ (100), and MgO(110) substrates, respectively, by magnetron sputtering at 300 °C. The base pressure is 2×10^{-5} Pa, and the growth rate is 0.12 nm/s using a Mn_2Au alloy target (atomic ratio, 2:1). High-resolution transmission electron microscopy (HRTEM) is carried out on a JEM-2100 electron microscope. Magnetic properties are measured using superconducting quantum-interference device (SQUID) magnetometry. X-ray absorption spectroscopy (XAS) and x-ray magnetic linear dichroism (XMLD) measurements in total-electron-yield mode are carried out at the beam line BL08U1A in the Shanghai Synchrotron Radiation Facility (at 300 K). The XAS spectra normalization is made by dividing the spectra by a factor such that the L_3 preedge and L_2 postedge have identical intensities for the two polarizations. After that, the preedge spectral region is set to zero and the peak at the L_3 edge is set to 1. Mn L-edge XMLD curves are characterized by the difference between linearly horizontal (||) and vertical (⊥) polarized x-ray absorption spectroscopy. The XMLD is measured at different in-plane rotation angles (θ), where θ is the angle between a crystalline axis of Mn_2Au and the horizontal polarization direction. Star devices for the SOT switching are fabricated using standard photolithography and argon-ion milling procedures. The writing current pulses of approximately 10^7 A cm^{-2} are generated by a Keysight B2961A source meter. After each writing pulse, a delay of 10 s is used for thermal relaxation, and a measurement of the transversal voltage across the central part of the patterned structure is then recorded when applying a reading current with a density of approximately 10^5 A cm^{-2} generated by an Agilent B2901A source meter.

The magnetic anisotropy energies (MAEs) for differently oriented Mn_2Au films are calculated using standard force theory (FT). The lattice constants of Mn_2Au on different substrates used in the calculations are obtained by x-ray-diffraction (XRD) experiments. The atomic position is fully relaxed. First, a self-consistence of electron charge density (electronic potential) is performed in the absence of spin-orbit coupling, followed by a one-step calculation with the presence of spin-orbit coupling when the magnetization is aligned along different axes. The band energy difference is evaluated as the MAE.

III. RESULTS

We first show the microstructure characterizations of 40-nm-thick Mn_2Au films in Fig. 1 with different epitaxial orientations grown by magnetron sputtering. XRD spectra show the (103), (101), and (204) textures for the Mn_2Au films grown on MgO(111), $SrTiO_3$ (100) and MgO(110) substrates, respectively, in the left panels of Figs. 1(a)–1(c). All of the films are single phase, with no evidence of a diffraction peak from second phases or other crystalline faces within the sensitivity of XRD measurements. Corresponding HRTEM images of the Mn_2Au films and different substrates cross sections are depicted in right panels of Fig. 1. There is no observation for grain boundaries in the overall films, though some point defects

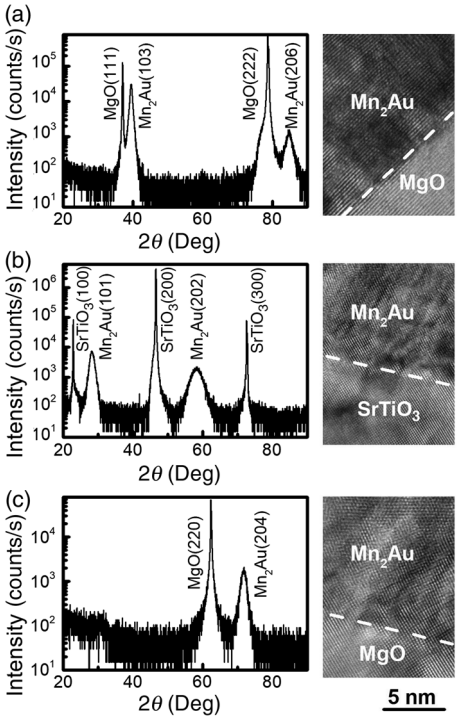

FIG. 1. Crystalline characterization of quasiepitaxial Mn_2Au films. (Left panels) XRD spectra and (right panels) concomitant HRTEM images for Mn_2Au (a) (103), (b) (101), and (c) (204) films deposited on the MgO(111), $SrTiO_3$ (100), and MgO(110) substrates, respectively.

still exist in the crystalline lattice, indicating the quasiepitaxial growth mode for the present Mn_2Au films through a simple sputtering method. The epitaxial growth mode provides a precondition for the observation of the orientation-dependent spin-orbit torque of Mn_2Au films, as discussed below.

We use SQUID magnetometry to check the antiferromagnetism of the Mn_2Au films. The magnetic field is applied in plane, i.e., parallel to the MgO-substrate (111) plane, [110] edge. Figure 2(a) presents the magnetization curves of the Mn_2Au (103) films at 300 K. Typical diamagnetic signals of up to 50 kOe are observed, which reflects the diamagnetic feature of the substrate, indicating the antiferromagnetism of the Mn_2Au (103) films without any ferromagnetic signal. Mn_2Au (101) and (204) films show similar behaviors. (See Figs. S1 and S2 of the Supplemental Material [32] for magnetization measurements.) Moreover, 5-nm-thick permalloy is deposited on top of the 10-nm Mn_2Au film to reaffirm the antiferromagnetism of the Mn_2Au (103) films. Corresponding magnetization data of $Mn_2Au(10\ nm)/permalloy(5\ nm)$ at 20 K, after 10 kOe of field cooling from 300 K, are depicted in Fig. 2(b). The hysteresis loop exhibits an apparent shift of 150 Oe compared to its coercivity of 400 Oe, indicating the antiferromagnetic order of the Mn_2Au (103) films. We then display a schematic of 3×3 unit cells of Mn_2Au (a Mn_2Si-type tetragonal structure with $a = b = 0.333$ nm and $c = 0.854$ nm) [33] in Fig. 2(c), where the Mn_2Au (103) plane is highlighted with a horizontal direction of [100] (a axis) and a vertical direction of $[0\bar{3}1]$. Also visible is the neighboring sublattice with an opposite magnetic moment, which is the prerequisite for the current-driven magnetic switching in Mn_2Au through spin-orbit torque.

To detect the switching of the Mn_2Au magnetic axis, the planar Hall resistance is obtained perpendicular to the reading current after two orthogonal writing currents are injected into the device alternatively. Figure 3(a) depicts a schematic of the star device and the current switching

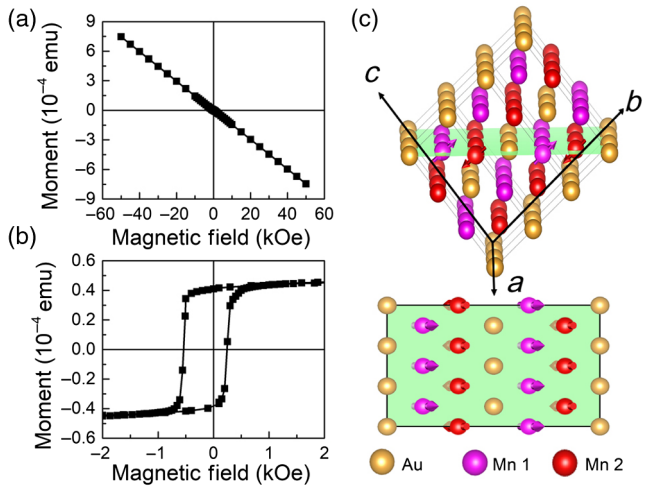

FIG. 2. Magnetic properties of Mn_2Au (103) films. The magnetic field is applied in plane, i.e., parallel to the MgO substrate (111) plane, [110] edge. (a) Magnetization curve of 40-nm Mn_2Au (103) films grown on MgO(111) substrates at 300 K. (b) Magnetic hysteresis loop of $Mn_2Au(10\ nm)/permalloy(5\ nm)$ bilayer at 20 K. (c) Schematic of 3×3 unit cells of Mn_2Au, where the Mn_2Au (103) plane is highlighted. The magnetic moments of the neighboring sublattices are opposing.

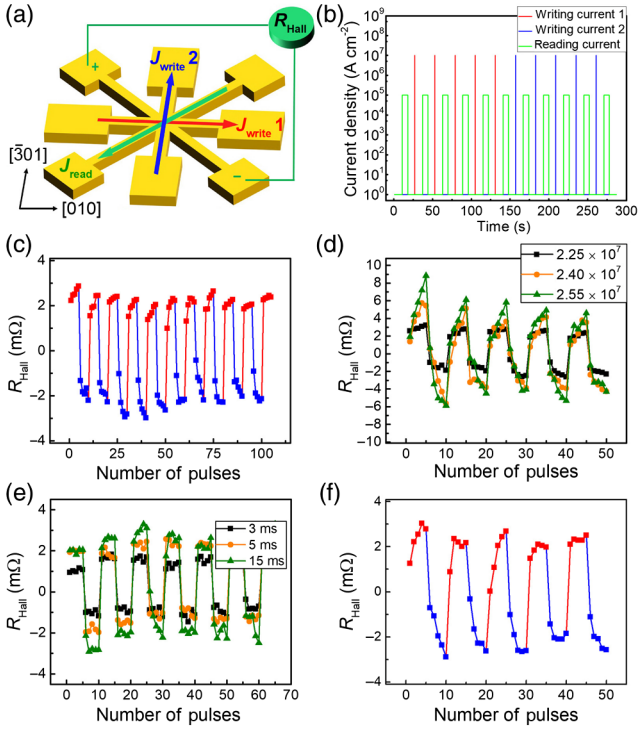

FIG. 3. Schematic of the switching measurement and current-driven switching of Mn_2Au (103) films. (a) Schematic of the star device and switching measurement geometry. Writing current pulses are applied along the red ($J_{write}1$) and blue arrows ($J_{write}2$) alternatively, corresponding to two orthogonal directions, [010] and [$\bar{3}$01], for Mn_2Au (103) films. The reading current is marked as the green arrow, while the concomitant Hall resistance is detected in its transverse direction. (b) Sketch of alternative writing current pulses along two orthogonal directions, $J_{write}1$ (red) and $J_{write}2$ (blue), of approximately 10^7 A cm^{-2}, and a reading current of about 10^5 A cm^{-2} (green) after each writing current pulse. (c) Hall resistance (R_{Hall}) change as a function of the number of writing current pulses. For Mn_2Au (103), five successive writing current pulses are applied along the [010] and [$\bar{3}$01] (blue) axes alternatively. After each writing current pulse, Hall resistance is recorded during the application of a reading current. The variation of R_{Hall} is shown by red and blue squares for the writing current pulse along [010] and [$\bar{3}$01], respectively. (d) Comparison of the variation of R_{Hall} with different magnitudes of writing current pulses. (e) Comparison of the variation of R_{Hall} with variable writing pulse widths. (f) The measurements of R_{Hall} are identical to (c), but both the writing current and reading current directions are rotated 45° from their counterparts in (c). All of the measurements are done at a sample temperature of 300 K, and a constant background of Hall resistance is subtracted.

measurement. For this experiment, five successive 1-ms-wide writing current pulses of $J_{write} = 2.10 \times 10^7$ A cm^{-2} are applied along the [010] axis (the red arrow, referred to as $J_{write}1$), and then along its vertical direction, the [$\bar{3}$01] axis (the blue arrow, $J_{write}2$) [Figs. 3(a) and 3(b)]. The current density is calculated with the following parameters: 42 mA applied writing current, 40-nm-thick Mn_2Au films, and a 5-μm width of the writing current arm of the star device. We record 10 s after each writing current pulse to release the possible tiny heat effect caused by the short current pulse of 1 ms. Then a reading current of $J_{read} = 4.17 \times 10^5$ A cm^{-2} is applied 45° away from the writing current, while the planar Hall resistance is recorded.

The [010]-directed writing pulses are expected to align a preference of domains with an AFM spin axis perpendicular to the [010] axis, and the writing current along the [$\bar{3}$01] direction then drives the magnetic switching back to the [010] axis. Following this concept, Fig. 3(c) shows the Hall resistance (R_{Hall}) variation as a function of the number of current pulses, five successive current pulses along the [010] and [$\bar{3}$01] axes alternatively [Fig. 3(b)]. The five current pulses along the [010] axis ($J_{write}1$) set the AFM spin axis perpendicular to the [010] axis, which gradually increases R_{Hall} to approximately 2.8 mΩ (the red squared line). Remarkably, a current pulse as short as 1 ms along [$\bar{3}$01] ($J_{write}2$) drives the AFM spins rotating back to the [010] direction, resulting in the R_{Hall} decreasing 4.4 mΩ to about -1.6 mΩ in the opposite sign. The following four pulses make the variation of R_{Hall} tend to be saturated (the blue squared line). After that, the five current pulses along the [010] axis increase R_{Hall}, which makes R_{Hall} reverse back to 2.6 mΩ in the vicinity of the initial 2.8 mΩ value. Note that a constant background is subtracted. Such a switching experiment is conducted in ten circles. Apparently, the R_{Hall} values increase and decrease without clear deterioration, indicating that the present magnetic switching is reversible, repeatable, and reliable.

The abrupt change of Hall resistance with the first current pulse, followed by gradually enhanced Hall resistance in the following four current pulses, reflects the multidomain switching feature of the present Néel-order SOT, which is quite characteristic for SOT in both the ferromagnetic system [34] and AFM Cu-Mn-As [5]. A temperature calibration is used to monitor the stability of the test temperature at 300 K, excluding the variation of resistance caused by temperature. It is worth mentioning that the Hall resistance is independent of the direction of the writing current, coinciding with the theory of current-driven switching of the AFMs [4]. Interestingly, the present switching is completed by a short current pulse of 1 ms, compared with the 50-ms pulse used in the Cu-Mn-As system [5], which reflects the strong switching capability of a metallic AFM system.

We then investigate the writing current density and the current-duration-time-dependent switching of the Mn_2Au films. Corresponding data are displayed in Figs. 3(d) and 3(e), respectively. For these experiments, different writing current densities (2.25×10^7, 2.40×10^7, and 2.55×10^7 A cm^{-2}) and current pulse widths (3, 5, and 15 ms) are applied to the star device. The measurement sequence is identical to that of Fig. 3(c). With an increasing writing current density and current duration time, the magnitude of R_{Hall} becomes larger, most likely due to stronger SOT switching by the applied current and the resultant 90° switching of the AFM moment. According to the current-induced switching results, the first and second pulses are decisive, which results in a sharp Hall-resistance change and major magnetic-moment switching, while following the writing pulses causes relatively small magnetic-moment switching and Hall-resistance variety. And the switching is reproducible during the five cycles. It should be mentioned that a much higher writing current and pulse width would induce nonrecyclable switching or device rupture through the thermal or electromigration effect. The current-induced switching results for different thicknesses reveal no thickness-dependent switching behavior, reflecting the calculated inherent switching ability of bulk Mn_2Au (see Fig. S3 of the Supplemental Material [32] for the thickness-dependent switching of Mn_2Au) [4,24,27].

In general, the antiferromagnets show magnetic anisotropy, which might affect the SOT switching. Thus, the switching capability of the Mn_2Au (103) films should be dependent on the current applied in different crystalline axes, besides two typical axes, [010] and [$\bar{3}$01]. We then explore the SOT effect when both the writing current and reading current directions are rotated 45° from their original counterparts. In this case, the direction of the writing current here is along the direction of the reading current in Fig. 3(a). It is interesting to find in Fig. 3(f) that R_{Hall} values also apparently increase and decrease without clear deterioration, and the recycling behavior for this switching is especially reliable. Also, the magnitude of R_{Hall} for the SOT switching is comparable to its counterpart in Fig. 3(c). The comparable SOT switching behaviors in Figs. 3(a) and 3(c) suggest that the Mn_2Au (103) films have no apparent antiferromagnetic easy axis.

The SOT switching experiments reveal that the AFM spins tend to arrange randomly and are comparable in each direction of (103)-orientation Mn_2Au. We now address the question of whether an analogous spin structure can also be detected by XMLD, which stands out as a unique method to identify the spin orientations in AFMs, despite the absence of a net moment [35,36]. Figure 4 presents Mn L-edge XMLD curves, characterized by the difference between linearly horizontal ($\parallel$) and vertical ($\perp$) polarized XAS (see Fig. S4 of the Supplemental Material [32] for the original XAS). The intensity of the XMLD is determined by the difference between the angles of the AFM spin and horizontal polarization and the AFM spin and vertical polarization: the larger the angle difference is, the stronger the XMLD signal is.

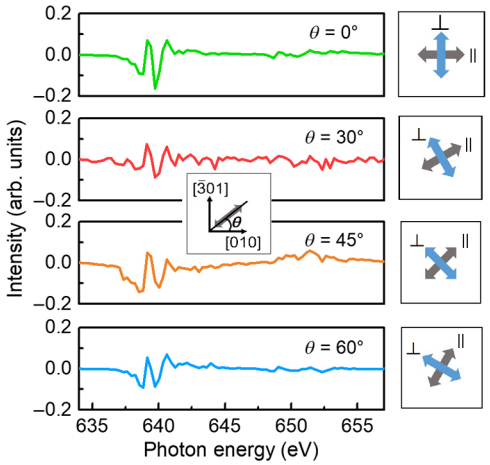

FIG. 4. Schematic of XMLD measurement and XMLD signals at different in-plane rotation angles (θ). (Left panels) XMLD signals at four typical angles between the horizontal polarized x-ray direction and the [010] axis of Mn_2Au ($\theta = 0°$, 30°, 45°, and 60°). (Right panels) Sketches of the rotation of the horizontal (||, gray solid arrows) polarized x ray and vertical (⊥, blue solid arrows) polarized x ray while the Mn_2Au [010] axis is set at $\theta = 0°$. The XMLD signals are measured at 300 K.

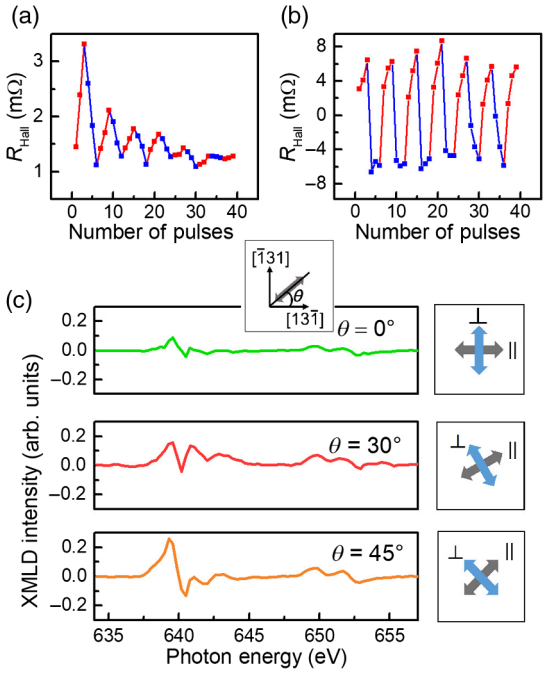

FIG. 5. SOT switching and spin-texture measurements of Mn_2Au (101) films. (a) Dependence of R_{Hall} variation on the number of writing current pulses. Three successive current pulses of $J_{write} = 2.00 \times 10^7$ A cm^{-2} are applied along the [13$\bar{1}$] and [$\bar{1}$31] axes alternatively. After each writing current pulse, R_{Hall} is recorded during application of the reading current of $J_{read} = 4.17 \times 10^5$ A cm^{-2}, which is denoted by red and blue squares corresponding to the writing current along the [13$\bar{1}$] and [$\bar{1}$31] axes, respectively. (b) The measurement procedure is the same as in (a), but the measurement configuration (both the writing current pulse and the reading current) is rotated 45° from the configuration in (a). (c) Schematic of XMLD measurement and XMLD signals under different in-plane rotation angles (θ). (Left panels) XMLD signals at three typical angles between the horizontal polarized x-ray direction and the [13$\bar{1}$] axis of Mn_2Au ($\theta = 0°$, 30°, and 45°). (Right panels) Sketches of the rotation of the horizontal (||, gray solid arrows) polarized x ray and the vertical (⊥, blue solid arrows) polarized x ray while the Mn_2Au [13$\bar{1}$] axis is set at $\theta = 0°$.

To understand the alignment of the AFM spins, the XMLDs at several typical angles (θ) are measured by changing the in-plane angle θ: the angle between the [010] axis of Mn_2Au and the horizontal polarization direction, as displayed in the inset of Fig. 4. For $\theta = 0°$, the horizontal polarized x ray is set to [010] axis of the Mn_2Au (103) films, while the vertical polarized x ray is along its vertical direction. The obtained XMLD signal is rather weak without characteristic "positive-to-negative" XMLD pattern at the L_3 edge (about 635–645 eV) [35]. Similar XMLD signals are observed for the spectra measured with $\theta = 30°$, 45°, and 60°, three typical directions between the [010] and [$\bar{3}$01] axes [see Fig. S5 of the Supplemental Material [32] for the pole figure of the Mn_2Au (103) films]. This finding demonstrates the absence of a dominant orientation for the ordered spin textures (Néel vectors) at the Mn_2Au (103) plane. This feature guarantees that the magnetic switching of Mn_2Au (103) is mainly determined by the vector with fieldlike torque, which realigns the spin texture perpendicular to the current channel on the basis of the theory [4]. The current applied alternatively at the [010] and [$\bar{3}$01] axes lead to the reversible modulation of AFM spins and the resultant planar Hall effect.

We then turn towards the SOT switching of Mn_2Au (101) films. The star devices for the Mn_2Au (101) films and the measurement setup are identical to those of Mn_2Au (103) in Fig. 3(a), but the crystal axis at $\theta = 0°$ is [13$\bar{1}$], and its vertical axis is [$\bar{1}$31] [see Fig. S6 of the Supplemental Material [32] for the pole figure of the Mn_2Au (101) films]. Figure 5(a) shows the Hall-resistance variation when four successive writing current pulses are applied alternatively along [13$\bar{1}$] (the red squares) and [$\bar{1}$31] (the blue squares) of the Mn_2Au (101) films. Note that R_{Hall} changes with the direction of the 1-ms-wide writing current pulse ($J_{write} = 2.00 \times 10^7$ A cm^{-2}) for the first circle. However, this variation attenuates seriously after the first circle, and it almost vanishes after five circles. These features reflect that the current cannot reversibly switch the AFM spin texture between the [13$\bar{1}$] and [$\bar{1}$31] axes. The situation turns out to be dramatically different when the probe configuration rotates 45°. That is, both the writing current and the reading current are rotated 45° from the origin case in Fig. 5(a). Corresponding data are presented in Fig. 5(b). R_{Hall} can be reversibly modulated by a writing current pulse with a 1-ms width and $J_{write} = 2.00 \times 10^7$ A cm^{-2}. This characterization

indicates that the AFM spin texture is switched between the [010] axis ($\theta = 45°$) and its vertical direction.

The transport measurements suggest that the spin texture of the Mn_2Au (101) films should be different from that of the Mn_2Au (103) films. Figure 5(c) depicts the XMLD spectra of three typical angles, $\theta = 0°$, 30°, and 45°, where the angle strongly affects the XMLD signal. For $\theta = 0°$, the horizontal and the vertical polarized x ray is set to the $[13\bar{1}]$ and $[\bar{1}31]$ axes of the Mn_2Au (101) films, respectively. It is found that the XMLD signal at the Mn L_3 edge is quite weak, indicating no obvious difference between $[13\bar{1}]$ and $[\bar{1}31]$. An analogous XMLD spectrum is obtained for $\theta = 30°$, but the magnitude of XMLD signals is somehow enhanced. The case differs completely as $\theta = 45°$. A characteristic positive-to-negative XMLD pattern at the L_3 edge indicates the distinguished spin textures between these two orientations, the [010] axis ($\theta = 45°$) and the $[\bar{1}01]$ axis ($\theta = 135°$). Because of the broken symmetry in the strained Mn_2Au films, the Néel vector orientation is most likely aligned along [010] ($\theta = 45°$) [7], making [010] an easy axis for the as-grown Mn_2Au (101) films. With the emergence of SOT by the writing current pulse along the [010] direction, the AFM spin texture can be switched to its vertical direction and then switch reversibly and flexibly between these two directions by applying alternative current pulses. However, for the hard axis of $[13\bar{1}]$ ($\theta = 0°$) or $[\bar{1}31]$ ($\theta = 90°$), the Néel vector orientation is difficult to arrange in these energy-disfavored directions. Even a part of spin texture is reluctant to be switched to these two directions by SOT, whereas the switching is hard to maintain because the AFM spins are pinned gradually by the easy axis [010] at $\theta = 45°$.

We then show the SOT switching and spin-texture measurements of Mn_2Au (204) films in Fig. 6. The experiments are carried out using the same procedure as that of the Mn_2Au (103) films in Fig. 3. One can see in Fig. 6(a) that the variation of Hall resistance is apparent when applying four successive 1-ms-wide writing current pulses of $J_{write} = 2.00 \times 10^7$ A cm^{-2} along the [010] ($\theta = 0°$, the red squares) and $[\bar{2}01]$ axes ($\theta = 90°$, the blue squares) alternatively [see Fig. S7 of the Supplemental Material [32] for the pole figure of the Mn_2Au (204) films]. The applied current along [010] initially aligns the AFM moments perpendicular to the current direction through the SOT effect and R_{Hall} turns out to increase. Then R_{Hall} turns out to decrease with the current along $[\bar{2}01]$, corresponding to the AFM switching back to the [010] axis. Two successive current pulses would saturate the variation of R_{Hall} to some extent. Remarkably, R_{Hall} values increase and decrease with ten series of current pulses along [010] and $[\bar{2}01]$, demonstrating the AFM moments are switched reversibly between the two perpendicular directions in the ten circles. The switching feature is completely different when the measurement configuration rotates 45°, i.e., the writing current pulses are applied at $\theta = 45°$. The variation of R_{Hall} is greatly

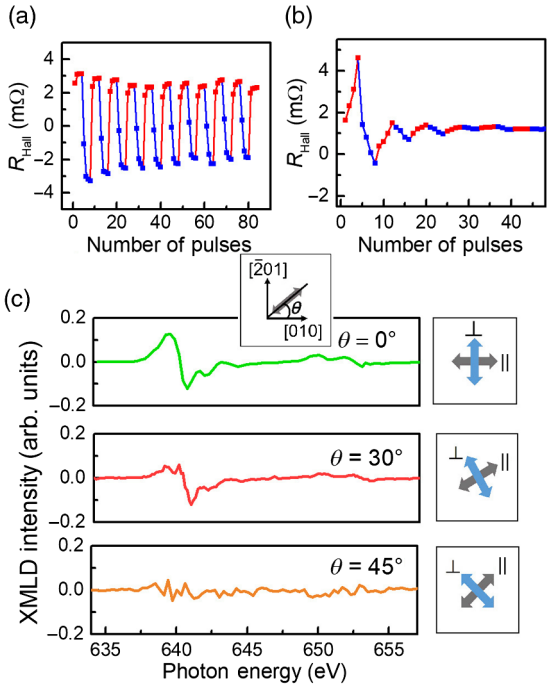

FIG. 6. SOT switching and spin-texture measurements of Mn_2Au (204) films. (a) Dependence of R_{Hall} on the number of writing current pulses. Four successive current pulses of $J_{write} = 2.00 \times 10^7$ A cm^{-2} are applied along the [010] and $[\bar{2}01]$ axes alternatively. After each writing current pulse, R_{Hall} is recorded during application of the reading current of $J_{read} = 4.17 \times 10^5$ A cm^{-2}, which is denoted by red and blue squares corresponding to the writing current along the [010] and $[\bar{2}01]$ axes, respectively. (b) The measurement procedure is the same as in (a), but the measurement configuration (both the writing current pulse and the reading current) is rotated 45° from the configuration in (a). (c) Schematic of XMLD measurement and XMLD signals under different in-plane rotation angles (θ). (Left panels) XMLD signals at three typical angles between the horizontal polarization direction and the [010] axis of Mn_2Au ($\theta = 0°$, 30°, and 45°). (Right panels) Sketches of the rotation of the horizontal (||, gray solid arrows) polarized x ray and vertical (⊥, blue solid arrows) polarized x ray while the Mn_2Au [010] axis is set at $\theta = 0°$.

reduced by increasing the cycling and remains unchanged after three switching circles. This feature reveals that the magnetic moments cannot be switched effectively in these two directions at $\theta = 45°$ and 135°.

XMLD signals in Fig. 6(c) support the transport measurements. For $\theta = 0°$, the horizontal and vertical polarized x rays are set to the [010] and $[\bar{2}01]$ axes of the Mn_2Au (204) films, respectively. Interestingly, the XMLD signal at $\theta = 0°$ features a characteristic positive-to-negative XMLD pattern at the L_3 edge, reflecting the easy axis along [010] for the as-grown Mn_2Au (204) films with strain induced by the MgO(110) substrates [37]. Accordingly, the XMLD signals at $\theta = 30°$ are greatly reduced, followed by the absence of the XMLD L_3-edge signal at $\theta = 45°$, reflecting

the fact that the spin textures strongly prefer to be aligned along the easy axis [010]. The Néel vectors are switched between [010] and its vertical direction. Such a strong AFM anisotropy is in a good agreement with the efficient switching between these two directions, followed by the comparatively easy SOT switching and speedy saturation of R_{Hall} in Fig. 6(a). By contrast, the SOT switching in the noneasy axis becomes more difficult with the fast attenuated variation of R_{Hall} in Fig. 6(b).

In addition, the Joule heat produced by a pulse-current electric current is simulated using finite-element modeling with COMSOL software. The instantaneous maximum temperature of the Mn_2Au device can increase from 300 to 424 K after a pulse of 2×10^7 A cm^{-2} amplitude and 1-ms length, which is far below the Néel temperature of Mn_2Au (>1000 K). Nevertheless, heat-assisted switching can play a role in reducing the current density, from an approximate theoretical value of $10^8 - 10^9$ A cm^{-2} [4] to about 10^7 A cm^{-2}. The electric-current-induced Oster field distribution is also simulated using finite-element modeling with COMSOL software. The maximum Oster field is only about 100 Oe. Such a disturbance of the magnetic field can be ignored for antiferromagnetic Mn_2Au (see Figs. S8 and S9 of the Supplemental Material [32] for the Joule heat and Oster field simulation).

IV. DISCUSSION

In order to understand the switching behavior in differently oriented Mn_2Au, the MAEs of differently oriented Mn_2Au films are calculated by using standard FT. According to the symmetry of bulk Mn_2Au, the MAEs can be expressed by [7]

$$E(\omega,\phi) = K_{2\perp}\sin^2\omega + K_{4\perp}\sin^4\omega + K_{4\parallel}\sin^4\omega\cos 4\phi. \quad (1)$$

Here, ω and φ are the angles between the magnetization ($\boldsymbol{M}$) and [001], as well as the projection direction of $\boldsymbol{M}$ on the Mn_2Au (001) plane and the [100] axis, respectively; $K_{2\perp}$, $K_{4\perp}$, and $K_{4\parallel}$ parametrize the uniaxial MAE constant, the fourth-order out-of-plane and in-plane MAE constants, respectively. Based on Eq. (1), the specific axes for the MAEs are listed as follows: $E([001]) = E(0,\varphi) = 0$, $E([100]) = E(\pi/2, 0) = K_{2\perp} + K_{4\perp} + K_{4\parallel} = E([010]) = E(\pi/2, \pi/2)$, and $E([110]) = E(\pi/2, \pi/4) = K_{2\perp} + K_{4\perp} - K_{4\parallel} = E([\bar{1}10]) = E(\pi/2, 3\pi/4)$. Apparently, the easy axis is determined by the sign of $K_{4\parallel}$. The easy axis is along [110] when $K_{4\parallel} > 0$ and [100] when $K_{4\parallel} < 0$. The lattice constants of the differently oriented Mn_2Au films used in the calculations are obtained using XRD experiments. Through first-principles calculations, the MAE constants $K_{2\perp}$, $K_{4\perp}$, and $K_{4\parallel}$ can be obtained according to the lattice constant and orientation (see Table S1 of the Supplemental Material [32] for the MAE constants), giving rise to the angular dependence of the MAEs in Fig. 7(a).

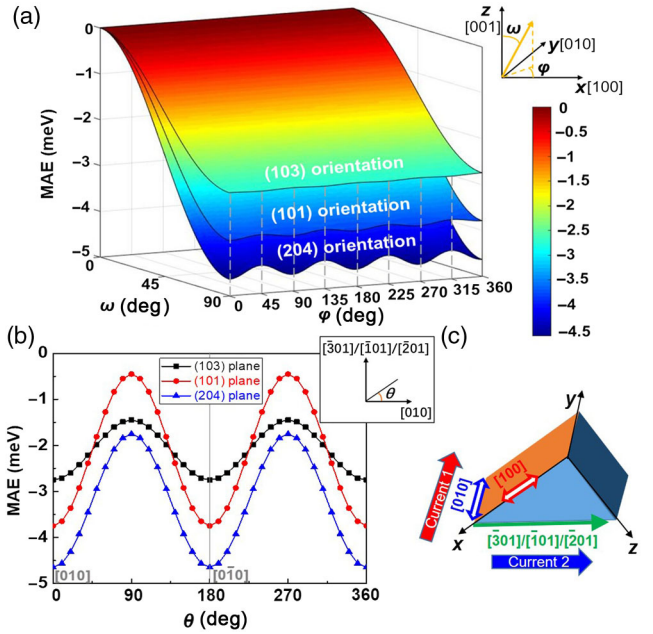

FIG. 7. MAE as a function of the magnetization direction (ω, φ) in Mn_2Au (103)-, (101)-, and (204)-oriented films. (a) MAEs of all space directions in Mn_2Au (103)-, (101)-, and (204)-oriented films. (b) MAE distribution as a function of in-plane angle θ with magnetizations lying in the (103), (101), and (204) planes, respectively. (c) Schematic of relationship between easy axes and current directions. Hollow double arrows represent the antiferromagnetic easy axes, and solid thick arrows represent the current directions. The gold plane represents the (001) plane, and the green arrow represents the projection of the [100] axis in the (103), (101), and (204) planes, respectively.

Note that MAE decreases with an increasing angle ω and becomes the lowest level for $\omega = 90°$, corresponding to Mn_2Au (001) plane, which is the easy magnetized plane. Concerning the details in the (001) easy plane, (103)-oriented Mn_2Au exhibits a negligible difference of MAE, accompanied by a comparable MAE value at $\varphi = 45°$ ([110]) and $\varphi = 90°$ (the [010] direction); thus, the magnetic moments of Mn_2Au (103) can be switched by current either between [100] and [010] or between [110] and [$\bar{1}$10], as illustrated in Fig. 3. The situation differs abruptly for (101)- and (204)-oriented Mn_2Au, the MAE is different when the magnetization rotates within the (001) plane, associated with a lower MAE at $\varphi = 0°$ ([100]) and 90° ([010]) than that at $\varphi = 45°$ ([110]) and 135° ([$\bar{1}$10]). Consequently, the magnetic moments of (101)- and (204)-oriented Mn_2Au can be switched by current between [100] and [010] rather than [110] and [$\bar{1}$10], as displayed in Figs. 5 and 6. An inspection of the MAEs of the Mn_2Au (103), (101), and (204) planes in Fig. 7(b) shows that the [010] direction ($\theta = 0°$) is indeed the energy minimum, whereas its vertical directions, [$\bar{3}$01], [$\bar{1}$01], and [$\bar{2}$01] for the (103), (101), and (204) planes, respectively, are the energy maxima. In this scenario, the magnetic-moment

switches between [010] and these directions are difficult. Instead, the magnetic moments are switched by two orthogonal currents between two easy axes, one being [010], lying within the (103), (101), and (204) planes, while the other easy axis, [100], lies out of these planes, as presented in Fig. 7(c). In fact, $[\bar{3}01]$, $[\bar{1}01]$, and $[\bar{2}01]$ can be considered at the respective projection of the [100] direction in the (103), (101), and (204) planes of Mn_2Au, which are parallel to their substrate surface. The variations of Hall resistances are read out by the planar Hall effect in the (103), (101), and (204) planes, respectively.

V. CONCLUSION

We demonstrate in this paper the spin-orbit torque in body-centered tetragonal antiferromagnet Mn_2Au with opposite-spin sublattices. There are five main features for the present findings: (i) The SOT switching behavior shows strong orientation dependence. The AFM moments are switched reversibly when the crystalline orientation plane has no strong magnetic anisotropy or the writing current is applied along the easy axis [010] and its vertical direction (the in-plane projection of the other easy axis [100] on the (101) and (204) plane), which is not only a typical feature for the SOT in AFM from the fundamental viewpoint but also provides a versatile candidate for antiferromagnet spintronics. (ii) Mn_2Au theoretically realizes sizable reorientations at current densities of approximately 10^8–10^9 A cm^{-2} [4]. We demonstrate the switching of Mn_2Au magnetic moments at current densities of about 10^7 A cm^{-2}, ascribed to the multidomain wall and heat-assisted switching. (iii) The growth parameter of quasiepitaxial Mn_2Au films by an easy-access magnetron sputtering method is optimized, where the buffer layer and molecular beam epitaxy are not necessary. (iv) SOT switching has been realized in Cu-Mn-As (arsenic-based semimetal), but only magnetic metals and alloys are generally considered for the electrode of magnetic tunnel junctions and relevant spintronics. Our work might advance the use of AFM alloys as a functional layer in spintronics. (v) SOT switching of an antiferromagnet occurs at room temperature, which is critical for the application of AFM spintronics. Our findings not only add an alternative dimension to spin-orbit torque but also represent a promising step towards antiferromagnet spintronics.

ACKNOWLEDGMENTS

We are grateful to Dr. Luqiao Liu of MIT for the fruitful discussions and the critical reading of the manuscript. We acknowledge the beam line BL08U1A in the Shanghai Synchrotron Radiation Facility (SSRF) for the XAS and XMLD measurements, and the Center for Testing and Analyzing of Materials for the technical support. We are grateful to the support by the Beijing Innovation Center for Future Chip. C. S. acknowledges the support of the Young Chang Jiang Scholars Program. This work was supported by the National Natural Science Foundation of China (Grants No. 51671110 and No. 51571128) and the National Key R&D Program of China (Grant No. 2017YFB0405704).

Note added.—Recently, we found two interesting works reporting current-induced switching in Mn_2Au [38,39]. The authors reported the SOT switching of Mn_2Au (001). It is significant that a large anisotropic magnetoresistance was observed in Ref. [38], a finding which deserves further extensive investigation.

[1] T. Jungwirth, X. Marti, P. Wadley, and J. Wunderlich, Antiferromagnetic spintronics, Nat. Nanotechnol. **11**, 231 (2016).
[2] W. Zhang and K. M. Krishnan, Epitaxial exchange-bias systems: From fundamentals to future spin-orbitronics, Mater. Sci. Eng. R **105**, 1 (2016).
[3] A. H. MacDonald and M. Tsoi, Antiferromagnetic metal spintronics, Phil. Trans. R. Soc. A **369**, 3098 (2011).
[4] J. Železný, H. Gao, K. Výborný, J. Zemen, J. Mašek, Aurélien Manchon, J. Wunderlich, Jairo Sinova, and T. Jungwirth, Relativistic Néel-Order Fields Induced by Electrical Current in Antiferromagnets, Phys. Rev. Lett. **113**, 157201 (2014).
[5] P. Wadley, B. Howells, J. Železný, C. Andrews, V. Hills, R. P. Campion, V. Novák, K. Olejník, F. Maccherozzi, S. S. Dhesi, S. Y. Martin, T. Wagner, J. Wunderlich, F. Freimuth, Y. Mokrousov, J. Kuneš, J. S. Chauhan, M. J. Grzybowski, A. W. Rushforth, K. W. Edmonds, B. L. Gallagher, and T. Jungwirth, Electrical switching of an antiferromagnet, Science **351**, 587 (2016).
[6] Y. Y. Wang, C. Song, B. Cui, G. Y. Wang, F. Zeng, and F. Pan, Room-Temperature Perpendicular Exchange Coupling and Tunneling Anisotropic Magnetoresistance in Antiferromagnet-Based Tunnel Junction, Phys. Rev. Lett. **109**, 137201 (2012).
[7] A. B. Shick, S. Khmelevskyi, O. N. Mryasov, J. Wunderlich, and T. Jungwirth, Spin-orbit coupling induced anisotropy effects in bimetallic antiferromagnets: A route towards antiferromagnetic spintronics, Phys. Rev. B **81**, 212409 (2010).
[8] S. Ikeda, K. Miura, H. Yamamoto, K. Mizunuma, H. D. Gan, M. Endo, S. Kanai, J. Hayakawa, F. Matsukura, and H. Ohno, A perpendicular-anisotropy CoFeB-MgO magnetic tunnel junction, Nat. Mater. **9**, 721 (2010).
[9] X. Marti, I. Fina, C. Frontera, J. Liu, P. Wadley, Q. He, R. J. Paull, J. D. Clarkson, J. Kudrnovský, I. Turek, J. Kuneš, D. Yi, J. H. Chu, C. T. Nelson, L. You, E. Arenholz, S. Salahuddin, J. Fontcuberta, T. Jungwirth, and R. Ramesh, Room-temperature antiferromagnetic memory resistor, Nat. Mater. **13**, 367 (2014).
[10] B. G. Park, J. Wunderlich, X. Martí, V. Holý, Y. Kurosaki, M. Yamada, H. Yamamoto, A. Nishide, J. Hayakawa, H. Takahashi, A. B. Shick, and T. Jungwirth, A spin-valve-like

magnetoresistance of an antiferromagnet-based tunnel junction, Nat. Mater. **10**, 347 (2011).

[11] A. Scholl, M. Liberati, E. Arenholz, H. Ohldag, and J. Stöhr, Creation of an Antiferromagnetic Exchange Spring, Phys. Rev. Lett. **92**, 247201 (2004).

[12] X. Z. Chen, J. F. Feng, Z. C. Wang, J. Zhang, X. Y. Zhong, C. Song, L. Jin, B. Zhang, F. Li, M. Jiang, Y. Z. Tan, X. J. Zhou, G. Y. Shi, X. F. Zhou, X. D. Han, S. C. Mao, Y. H. Chen, X. F. Han, and F. Pan, Tunneling anisotropic magnetoresistance driven by magnetic phase transition, Nat. Commun. **8**, 449 (2017).

[13] R. O. Cherifi, V. Ivanovskaya, L. C. Phillips, A. Zobelli, I. C. Infante, E. Jacquet, V. Garcia, S. Fusil, P. R. Briddon, N. Guiblin, A. Mougin, A. A. Ünal, F. Kronast, S. Valencia, B. Dkhil, A. Barthélémy, and M. Bibes, Electric-field control of magnetic order above room temperature, Nat. Mater. **13**, 345 (2014).

[14] J. Nogués and I. K. Schuller, Exchange bias, J. Magn. Magn. Mater. **192**, 203 (1999).

[15] A. Scholl, M. Liberati, E. Arenholz, H. Ohldag, and J. Stöhr, Creation of an Antiferromagnetic Exchange Spring, Phys. Rev. Lett. **92**, 247201 (2004).

[16] Y. Y. Wang, X. Zhou, C. Song, Y. N. Yan, S. M. Zhou, G. Y. Wang, C. Chen, F. Zeng, and F. Pan, Electrical control of exchange spring in antiferromagnetic metals, Adv. Mater. **27**, 3196 (2015).

[17] T. Zhao, A. Scholl, F. Zavaliche, K. Lee, M. Barry, A. Doran, M. P. Cruz, Y. H. Chu, C. Ederer, N. A. Spaldin, R. R. Das, D. M. Kim, S. H. Baek, C. B. Eom, and R. Ramesh, Electrical control of antiferromagnetic domains in multiferroic $BiFeO_3$ films at room temperature, Nat. Mater. **5**, 823 (2006).

[18] C. Song, B. Cui, F. Li, X. Zhou, and F. Pan, Recent progress in voltage control of magnetism: Materials, mechanisms, and performance, Prog. Mater. Sci. **87**, 33 (2017).

[19] C. Song, Y. F. You, X. Z. Chen, X. F. Zhou, Y. Y. Wang, and F. Pan, How to manipulate magnetic states of antiferromagnets, Nanotechnology **29**, 112001 (2018).

[20] M. J. Grzybowski, P. Wadley, K. W. Edmonds, R. Beardsley, V. Hills, R. P. Campion, B. L. Gallagher, J. S. Chauhan, V. Novak, T. Jungwirth, F. Maccherozzi, and S. S. Dhesi, Imaging Current-Induced Switching of Antiferromagnetic Domains in CuMnAs, Phys. Rev. Lett. **118**, 057701 (2017).

[21] D. C. Ralpha and M. D. Stilesb, Spin transfer torques, J. Magn. Magn. Mater. **320**, 1190 (2008).

[22] L. Liu, C. F. Pai, Y. Li, H. W. Tseng, D. C. Ralph, and R. A. Buhrman, Spin-torque switching with the giant spin Hall effect of tantalum, Science **336**, 555 (2012).

[23] Y. B. Fan, P. Upadhyaya, X. F. Kou, M. R. Lang, S. Takei, Z. Wang, J. S. Tang, L. He, L. T. Chang, M. Montazeri, and K. L. Wang, Magnetization switching through giant spin-orbit torque in a magnetically doped topological insulator heterostructure, Nat. Mater. **13**, 699 (2014).

[24] J. Železný, H. Gao, A. Manchon, F. Freimuth, Y. Mokrousov, J. Zemen, J. Mašek, J. Sinova, and T. Jungwirth, Spin-orbit torques in locally and globally noncentrosymmetric crystals: Antiferromagnets and ferromagnets, Phys. Rev. B **95**, 014403 (2017).

[25] C. Bi, H. Almasi, K. Price, T. Newhouse-Illige, M. Xu, S. R. Allen, X. Fan, and W. Wang, Anomalous spin-orbit torque switching in synthetic antiferromagnets, Phys. Rev. B **95**, 104434 (2017).

[26] G. Y. Shi, C. H. Wan, Y. S. Chang, F. Li, X. J. Zhou, P. X. Zhang, J. W. Cai, X. F. Han, F. Pan, and C. Song, Spin-orbit torque in MgO/CoFeB/Ta/CoFeB/MgO symmetric structure with interlayer antiferromagnetic coupling, Phys. Rev. B **95**, 104435 (2017).

[27] V. M. T. S. Barthem, C. V. Colin, H. Mayaffre, M. H. Julien, and D. Givord, Revealing the properties of Mn_2Au for antiferromagnetic spintronics, Nat. Commun. **4**, 2892 (2013).

[28] W. Zhang, W. Han, S. H. Yang, Y. Sun, Y. Zhang, B. Yan, and S. S. P. Parkin, Giant facet dependent spin-orbit torque and spin Hall conductivity in the triangular antiferromagnet $IrMn_3$, Sci. Adv. **2**, e1600759 (2016).

[29] H. C. Wu, Z. M. Liao, R. G. Sumesh Sofin, G. Feng, X. M. Ma, A. B. Shick, O. N. Mryasov, and I. V. Shvets, Mn_2Au: Body-centered-tetragonal bimetallic antiferromagnets grown by molecular beam epitaxy, Adv. Mater. **24**, 6374 (2012).

[30] H. C. Wu, M. Abid, A. Kalitsov, P. Zarzhitsky, M. Abid, Z. M. Liao, C. Ó. Coileáin, H. Xu, J. J. Wang, H. Liu, O. N. Mryasov, C. R. Chang, and I. V. Shvets, Anomalous anisotropic magnetoresistance of antiferromagnetic epitaxial bimetallic films: Mn_2Au and Mn_2Au/Fe bilayers, Adv. Funct. Mater. **26**, 5884 (2016).

[31] M. Jourdan, H. Bräuning, A. Sapozhnik, H. J. Elmers, H. Zabel, and M. Kläui, Epitaxial Mn_2Au thin films for antiferromagnetic spintronics, J. Phys. D **48**, 385001 (2015).

[32] See Supplemental Material at http://link.aps.org/supplemental/10.1103/PhysRevApplied.9.054028 for experimental details; magnetic properties of Mn_2Au (101) and (204) films; different-thickness (103)-oriented Mn_2Au switching behavior; raw data for XAS; pole figures for Mn_2Au (103), (101), and (204) films; Joule heat and Oster field simulation; and magnetocrystalline anisotropy energy parameters.

[33] R. Masrourab, E. K. Hlilc, M. Hamedound, A. Benyoussefbde, A. Boutaharf, and H. Lassrif, Antiferromagnetic spintronics of Mn_2Au: An experiment, first principle, mean field and series expansions calculations study, J. Magn. Magn. Mater. **393**, 600 (2015).

[34] O. J. Lee, L. Q. Liu, C. F. Pai, Y. Li, H. W. Tseng, P. G. Gowtham, J. P. Park, D. C. Ralph, and R. A. Buhrman, Central role of domain wall depinning for perpendicular magnetization switching driven by spin torque from the spin Hall effect, Phys. Rev. B **89**, 024418 (2014).

[35] B. Cui, F. Li, C. Song, J. J. Peng, M. S. Saleem, Y. D. Gu, S. N. Li, K. L. Wang, and F. Pan, Insight into the antiferromagnetic structure manipulated by electronic reconstruction, Phys. Rev. B **94**, 134403 (2016).

[36] L. J. Zhang, Z. J. Xu, X. Z. Zhang, H. N. Yu, Y. Zou, Z. Guo, X. J. Zhen, J. F. Cao, X. Y. Meng, J. Q. Li, Z. H. Chen, Y. Wang, and R. Z. Tai, Latest advances in soft x-ray spectromicroscopy at SSRF, Nucl. Sci. Technol. **26**, 040101 (2015).

[37] A. A. Sapozhnik, R. Abrudan, Yu. Skourski, M. Jourdan, H. Zabel, M. Kläui, and H. J. Elmers, Manipulation of antiferromagnetic domain distribution in Mn_2Au by ultrahigh magnetic fields and by strain, Phys. Status Solidi RRL **11**, 1600438 (2017).

[38] S. Yu. Bodnar, L. Šmejkal, I. Turek, T. Jungwirth, O. Gomonay, J. Sinova, A. A. Sapozhnik, H. J. Elmers, M. Kläui, and M. Jourdan, Writing and reading antiferromagnetic Mn_2Au: Néel spin-orbit torques and large anisotropic magnetoresistance, Nat. Commun. **9**, 348 (2018).

[39] M. Meinert, D. Graulich, and T. Matalla-Wagner, Key role of thermal activation in the electrical switching of antiferromagnetic Mn_2Au, arXiv:1706.06983.